Lithium Niobate Crystal with Embedded Au Nanoparticles: A New Saturable Absorber for Efficient Mode-Locking of Ultrafast Laser Pulses at 1 μm

Pang, C.; Li, R.; Li, Z.; Dong, N.; Cheng, C.; Nie, W.; Böttger, R.; Zhou, S.; Wang, J.; Chen, F.;

Originally published:

May 2018

Advanced Optical Materials 16(2018), 1870065

DOI: https://doi.org/10.1002/adom.201800357

Title Lithium niobate crystal embedded with Au nanoparticles: A new saturable absorber for efficient mode-locking of ultrafast laser pulses at 1μm

*Chi Pang, Rang Li, Ziqi Li, Ningning Dong, Chen Cheng, Weijie Nie, Roman Böttger, Shengqiang Zhou, Jun Wang, and Feng Chen**

C. Pang, R. Li, Z.Q. Li, C. Cheng, W.J. Nie, Prof. F. Chen

School of Physics, State Key Laboratory of Crystal Materials, Key Laboratory of Particle Physics and Particle Irradiation

Shandong University

Jinan 250100, China

Email: drfchen@sdu.edu.cn

Dr. N. N. Dong, Prof. J. Wang

Key Laboratory of Materials for High-Power Laser

Shanghai Institute of Optics and Fine Mechanics

Chinese Academy of Sciences

Shanghai 201800, China

Dr. R. Böttger, Dr. S.Q. Zhou

Helmholtz-Zentrum Dresden-Rossendorf

Institute of Ion Beam and Materials Research

Bautzner Landstrasse 400, Dresden 01328, Germany

Keywords: plasmonic Au nanoparticles, lithium niobate crystals, ion implantation, saturable absorbers, mode-locked lasers

We report on plasmonic Au nanoparticles embedded in $LiNbO_3$ crystals as efficient saturable absorbers to realize 74.1 ps mode-locked laser pulse generation at 1 μm. The system has been fabricated by Au ion implantation and post annealing, a well-developed chip-technology. The

strong optical absorption band peaking at 640 nm is observed due to the localized surface plasmonic resonance (LSPR) effect. The Z-scan investigation shows that the $LiNbO_3$ crystals embedded with Au nanoparticles possess ultrafast saturable absorption properties at near infrared 1μm wavelength. With this feature we apply the Au nanoparticles embedded $LiNbO_3$ wafer as saturable absorber into a laser-written Nd:YVO_4 waveguide platform. We obtain stable laser pulses at 1064 nm based on the efficient passive Q-switched mode-locking process, reaching repetition rate of 6.4 GHz and pulse duration of 74.1 ps. Since $LiNbO_3$ has broadband applications in various optical systems, this work opens the way of developing intriguing devices in $LiNbO_3$-based photonic circuits by using embedded metallic nanoparticles.

Lithium niobate ($LiNbO_3$) is one of most favorite multifunctional crystals owing to its unique features consisting of excellent electro-optic, nonlinear optical, photorefractive, acousto-optic, ferroelectric, and piezoelectric properties, which enable $LiNbO_3$-based devices, in configurations of bulks or waveguides, for wide applications in various areas.[1-3] For examples, rare-earth (Er^{3+} or Nd^{3+}) ion doped $LiNbO_3$ could serve as platforms for optical amplification or lasing.[4,5] Periodically poled $LiNbO_3$ crystal wafers are excellent media for frequency conversion of broadband wavelength regimes for nonlinear optical applications.[6,7] The commercial available electro-optic modulators have been manufactured on base of $LiNbO_3$ wafers or waveguides, reaching high-speed modulation of tens of GHz bandwidth.[8-11] The recent development of thin-film $LiNbO_3$ (lithium niobate on insulators or silicon) technology offers possibility to produce crystalline ultrathin films with thickness down to 50 nm, in which much more compact devices (microring resonators, photonic crystal slabs, photonic nanowires etc.) could be constructed for a number of promising applications.[12-14] Moreover, the integration of multi-components in a monolithic $LiNbO_3$ chip will be much attractive for both scientific research and industries,[15-19] e.g., as integrated quantum

circuits.[20] Therefore, additional functions of $LiNbO_3$ crystals deserve further exploration in order to develop more intricate devices.

Metallic nanoparticles (NPs) have attracted great attentions of researchers in a variety of areas owing to the so-called localized surface plasmonic resonance (LSPR) effect excited by light irradiation of NPs smaller than light wavelength.[21-25] Particularly, noble-metal NPs (e.g., Au, Ag) have been widely applied in diverse systems to implement intriguing applications in biosensing, imaging, diagnostic/therapy, and photocatalysts.[26-33] In laser technology, NPs or other nanostructures (nanorods or nanopyramids) may serve as effective saturable absorbers (SAs) for laser pulse generation through the passive Q-switching or mode-locking configurations.[34-37] Towards to this purpose, by using chemical synthesis, the Au-nanostructure-based SAs have been produced and ultrafast laser pulses have been realized in bulk or fiber laser systems.[38] In addition to chemical methods, the ion beam technology offers alternative solutions for noble-metal NPs fabrication. On one hand, the direct implantation of noble-metal ions (such as Au^+, Ag^+) can be used to synthesize NPs with spherical geometries into dielectrics; one the other band, by using swift heavy ion irradiation, spherical NPs could be elongated to be nanorods with efficient reshaping of nanostructures.[39-43] The concentration of NPs can be controlled by ion fluences/doses and post-implantation annealing treatment. Nevertheless, most work on the exploration of metallic NPs was focused on glass substrates, [44-46] whilst, in crystals with diverse lattice structures, the investigation on their synthesis and applications is very limited.[47,48] Recently, we reported on the synthesis of Au and Ag NPs embedded in Nd:YAG single crystals, and observed giant enhancement of third-order optical nonlinearities in the visible light band due to the LSPR effects. With the LSPR-induced saturable absorption, the stable laser pulses at 639 nm (within the main LSPR band) has been achieved by using a $Pr:LuLiF_4$ crystal as gain medium.[49] Since the LSPR band of noble-metal NPs is mainly located at visible light wavelength, the application of NPs embedded in insulators is limited for longer wavelength. In this work, we use a novel SA, i.e.,

Au NPs embedded $LiNbO_3$ crystal (hereafter abbreviated by AuNP:LN), which is synthesized by direct Au ion implantation. The saturable absorption at near-infrared (NIR) wavelength of 1μm has been observed as the concentration of NPs is above a threshold, which may be due to the synergy effect of Au NPs and the $LiNbO_3$ substrate from their separate optical nonlinearities, and this phenomenon was absent from any isotropic matrix (e.g., glasses or cubic Nd:YAG crystal). Based on this feature, the 1μm laser pulses with a as short as 74-ps duration are generated from a laser-written Nd:YVO_4 waveguide cavity through passive Q-switched mode-locking with AuNP:LN wafer as SA. In addition to this extension of SA to NIR band pulsed lasing, another significant advantage is that the $LiNbO_3$-based SAs would have superior capability to be connected with other components to construct intricate devices for diverse applications.[50,51]

The transmission electronic microscopy (TEM) has been applied to investigate the Au NPs embedded in the $LiNbO_3$ crystal. **Figure 1**a shows the cross-sectional TEM micrograph of the sample, in which Au NPs with an average diameter of 30 nm locate in the near surface of crystal. The distribution of NPs' diameters is displayed in Figure 1b. In order to obtain further information of Au NPs, High Resolution Transmission Electron Microscopy (HRTEM) is utilized to image the details of the area A marked in Figure 1a. As shown in Figure 1c of the HRTEM image, some small NPs (diameters less than 2 nm) are in the vicinity of a large NP. This phenomenon containing one large NP surrounded by a number of small NPs exists widely in the present AuNP:LN system. Nevertheless, the amount of these small NPs is considerably large, which cannot be counted. The HRTEM image of the region marked as B in Figure 1c shows the crystallization of Au NPs with interplanar spacing *d* of 2.204 nm, which is consistent with (202) $LiNbO_3$. The crystalline phase is further indicated by the corresponding FFT pattern (Figure 1d) of the individual NP as well as the SAED pattern (Figure 1e). As illustrated in Figure 1f, qualitative chemical analysis has been performed by energy dispersive X-ray spectroscopy (EDXS), which further confirms the formation of Au

NPs in the $LiNbO_3$ crystal. It should be also pointed out that the depth profile of the Au ions could be calculated by the code of Stopping and Range of Ions in Matter (SRIM) (see supporting information: Figure S1).[52] Compared with the calculation, the Au NPs move towards the $LiNbO_3$ surface (out-diffusion effect) during the thermal annealing process.[53]

As illustrated in **Figure 2**a, the near field enhancement of AuNP:LN is calculated by numerically solving the Maxwell's equations using the discrete dipole approximation (DDA) as implemented in the DDSCAT code.[54] The Au nanospheres with diameters of 30 nm in a $LiNbO_3$ crystal cube comparable with experimentally prepared samples are used in our calculations, and air is used as the external medium. It can be seen that the high optical electric field intensity is mainly distributed around the NPs and in the outside surface of crystal, which indicates the essential effect of the margin of $LiNbO_3$ crystal. Figure 2b shows the absorption spectrum of NPs before and after annealing, indicating the occurrence of LSPR effect. In addition, one can clearly see that the main absorption peak shows red shift after annealing. Fitting of the absorption of a single NP based on Mie theory is less accurate in this case as it only offers calculation of NPs with discrete values of different diameters (see more details are exhibited in Supporting Information (Figure S2d)). To facilitate our interpretation, the relative structures of Au NPs, the $LiNbO_3$ substrate and the coordinates used in this work are shown in Figure 2d, in which a few small NPs with diameters of 2 nm are around a large NP with a large scale (30 nm) in the $LiNbO_3$ crystal. The electric field distributions of NPs at different wavelengths (550, 640, 750, 850, 950, 1064 nm) are calculated, respectively (Figure 2d). As one can see, the optical limiting of NPs is dependent on particle sizes as well as excitation wavelengths. At short wavelength, the larger NP exhibits stronger limiting of light. The range of high electric field caused by the large NP covers surrounding small NPs; as a result, the effect from the larger NP is dominant in comparison to NPs with small scales. Whilst in the longer wavelength band (e.g., near infrared, NIR), the effect of large NPs becomes significantly weak, which enables smaller NPs to play innegligible roles in limiting

light. We introduce an influence factor a_i to fit the absorption γ_{sum} before and after 640 nm through Mie theory (see more details in Supporting Information (Figure S2e)):

$$\gamma_i = \frac{18\pi p\varepsilon_d^{3/2}}{\lambda_0} \frac{\varepsilon_m^{"}}{|\varepsilon_m + 2\varepsilon_d|^2} \quad (1)$$

$$\sum a_i \gamma_i = \gamma_{sum} \quad (2)$$

where ε_m, ε_d and p are the complex dielectric constants of metal and insulator, and the volume fraction of metal, respectively. $\varepsilon_m^{"}$ and λ_0 denote the imaginary part of ε_m and the wavelength of light in vacuum. a_i and γ_i represent the influence factor and absorption of NPs with diameters i, respectively.[55] Figure 2c reveals the result of the fitted absorption, which is in reasonable agreement with the experimental results (Figure 2b).

We use the well-known Z-scan technique to investigate the nonlinear optical properties of AuNP:LN system. In the visible band, the AuNP:LN exhibits a reverse saturable absorption (RSA) because of the synergistic effect between strong RSA of $LiNbO_3$ and relatively weak saturable absorption of Au NPs (Figure S3). However, in the NIR band, the RSA effect of $LiNbO_3$ becomes significantly degraded. **Figure 3**a shows the result of the open Z-scan measurement of the $LiNbO_3$ crystal at 1030 nm. This negligible RSA of $LiNbO_3$ offers a possibility to generate the saturable absorption effect of the AuNP:LN system at the NIR wavelength band. From the obtained Z-scan data of the AuNP:LN (Figure 3b-f), obvious ultrafast saturable absorption curves have been observed, indicating opposite nonlinear absorption of the AuNP:LN system at NIR to that of visible band. For a system with obvious saturable absorption response, the propagation equation can be written as

$$\frac{dI}{dz} = -(\alpha_0 + \beta_{eff} \cdot I) \cdot I \quad (3)$$

where I is the saturation intensity, α_0 is the linear absorption coefficient, β_{eff} is the nonlinear absorption coefficient, and z is the distance along the laser propagation direction. This equation can be solved as follows:

$$T_{Norm}(z) = \frac{\ln[1+q_0(z)]}{q_0(z)} \quad (4)$$

where $q_0(z) = \beta_{eff}(I_0 L_{eff})/(1+z^2/z_0^2)$, $L_{eff} = [1-e^{-\alpha_0 L}]/\alpha_0$, L_{eff} is the effective thickness of the Au NPs layer, L is the Au NPs layer thickness, I_0 is the light intensity at the focus, and z_0 is the beam's diffraction length.[56] By fitting the open-aperture Z-scan results, we can obtain the β_{eff} of these samples, and the negative value represents the SA response. Based on Equation 4, the variation of the nonlinear absorption coefficient with the energy of the excited pulse is displayed in **Table** 1. The nonlinear absorption coefficient increases from -130.2 cm/GW to -24.2 cm/GW with the enhancement of the excitation energy.

One of the main applications of materials with ultrafast saturable absorption nonlinearities is to generate pulsed lasers through passive Q-switching or mode-locking configuration. We have used AuNP:LN as a SA into a laser-written Nd:YVO_4 waveguide system to implement a stable Q-switched mode-locking laser at wavelength of 1064nm. **Figure 4**a shows the schematic diagram of the experimental arrangement for the Q-switched mode-locking generation. Figure 4b reveals the average output power as a function of incident power along TE and TM polarization. The obtained lasing threshold is 75.6 mW (119.7 mW) with the maximum output average power of 58.6 mW (32.9 mW) at TE- (TM-) polarization. The slope

efficiencies are of 13.6% and 8.5% for the TE- or TM-polarization, respectively (see more details about characterization of Q-switched pulsed laser in Supporting Information (Figure S4)). Figure 4c manifests that the central wavelength of the pulsed laser is 1064 nm, which corresponds to the the transition $^4F_{3/2} \rightarrow 4I_{9/2}$ of Nd^{3+} ions. Inserts of Figure 4c depict the typical pulse trains of the Q-switched laser at TE- and TM-polarized pump. A single Q-switching envelope containing mode-locking pulses is presented in Figure 4d. As illustrated in Figure 4e, the repetition rate of the mode-locking is determined to be 6.4 GHz and the pulse duration is 74.1 ps.

In summary, we report on the synthesis of Au NPs embedded in $LiNbO_3$ by using direct Au ion implantation. The nonlinear optical properties of the AuNP:LN system have been investigated, which indicates opposite features at the visible and NIR wavelength band. Particularly, ultrafast saturable absorption has been observed for the AuNP:LN system at 1 μm, which shows potential applications as saturable absorbers to generate ultrafast lasing. Finally, the AuNP:LN based Q-switched mode-locked lasing has been implemented in the Nd:YVO_4 waveguide system, reaching 1μm laser pulses with the repetition rate of 6.4 GHz and the pulse duration of 74.1 ps. Since $LiNbO_3$ has broadband applications in various optical systems, this work not only opens the way of developing intriguing devices in $LiNbO_3$-based photonic circuits by using embedded metallic NPs, but also manifests the significant potential of $LiNbO_3$ with NPs for ultrafast lasers and integrated photonic devices.

Experimental Section

Synthesis of Au NPs: The *z*-cut $LiNbO_3$ crystal wafer was cut into 10×10×1 mm^3 and optically polished. The Au^+ ions at energy of 180 keV and fluence of 3×10^{16} ions/cm^2 were implanted into $LiNbO_3$ crystals from one face of 10×10 mm^2 at room temperature at the Ion Beam Centre of Helmholtz-Zentrum Dresden-Rossendorf, Germany. After implantation, the sample was annealed at 1000°C for 1h in air. With this processing, the AuNP:LN wafer was produced.

Characterization of Au NPs: TEM investigations were carried out with FEI Tecnai G2 F20 S-TWIN operated at an accelerating voltage of 200 kV, with the point resolution 0.24 nm, the line resolution 0.102 nm and the information resolution 0.14 nm. The sample was glued by M-bond 610 and scaled down to less than 20 μm by double-sided lapping. The Precision Ion Polishing System (Gatan691) was reduced from 4.8 kV to 3.2 kV by degrees, meanwhile, the dip angle was decreased gradually from 10° to 4°. The absoprtion spectrum of the prepared samples were measured by using a UV-VIS-NIR spectrophotometer (Hitachi, U-4100) from 400 nm to 1000 nm.

Z-scan measurement: The arrangement of the open-aperture Z-scan apparatus is shown in Supporting Information. The saturable absorption of Au NPs was detected by the open-aperture Z-scan system, which was widely employed to investigate the nonlinear optical response. The experiment was carried out by using mode-locked fiber laser at 1030 nm, with the repetition rate of 1 kHz and the pulse width of 340 fs. The beam waist radius at the focus was ~30 μm at 1030 nm. Sample placed on the motorized platform was moved gradually along the propagation direction of the incident laser. Meanwhile, the transmittance through the sample as a function of laser intensity was measured. The schematic of the experimental arrangement of the Z-scan system can be seen in Figure S5.

Q-switched mode-locking operation: As shown in Figure 1b, the pulsed laser experiment was carried out by using the end-face coupling arrangement with the pump from a linearly polarized light beam at 808 nm, which was generated from a tunable CW Ti:sapphire (Coherent MBR-PE) laser. A half-wave plate was utilized to convert the polarization of the launched light. A spherical convex lens (focal length of 30 mm) was used to couple the pump laser into the waveguide through the sample, which was clamped tightly by the input mirror (with high transmission of 98% at 808 nm and high reflectivity > 99% at 1064 nm) and the end-face of the waveguide. A digital oscilloscope (Tektronix, MSO72504DX) was used to

display the image of pulsed laser from the output face of the waveguide, which was collected by a 20× microscope objective mirror.

Supporting Information
Supporting Information is available from the Wiley Online Library or from the author.

Acknowledgements
This work was supported by National Natural Science Foundation of China (NSFC) (11535008); National Natural Science Foundation of China (61522510); STCSM Excellent Academic Leader of Shanghai (17XD1403900).

Received: ((will be filled in by the editorial staff))
Revised: ((will be filled in by the editorial staff))
Published online: ((will be filled in by the editorial staff))

Conflict of Interest
The authors declare no conflict of interest.

References

[1] K. Lengyel, Á. Péter, L. Kovács, G. Corradi, L. Pálfalvi, J. Hebling, M. Unferdorben, G. Dravecz, I. Hajdara, Z. Szaller, K. Polgár, *Appl. Phys. Rev.* **2015**, *2*, 040601.

[2] C. Paillard, X. Bai, I. C. Infante, M. Guennou, G. Geneste, M. Alexe, J. Kreisel, B. Dkhil, *Adv. Mater.* **2016**, *28*, 5153.

[3] F. Chen, J. R. V. de Aldana, *Laser Photonics Rev.* **2014**, *8*, 251.

[4] D. Brüske, S. Suntsov, C. E. Rüter, D. Kip, *Opt. Express* **2017**, *25*, 29374.

[5] D. Z. Wang, D. H. Sun, X. L. Kang, Y. H. Sang, B. X. Yan, H. Liu, Y. Bi, *Opt. Express* **2015**, *23*, 17727.

[6] G. Li, Y. Chen, H. Jiang, X. Chen, *Opt. Lett.* **2017**, *42*, 939.

[7] M. Bock, A. Lenhard, C. Chunnilall, C. Becher, *Opt. Express* **2016**, *24*, 23992.

[8] A. J. Mercante, P. Yao, S. Shi, G. Schneider, J. Murakowski, D. W. Prather, *Opt. Express* **2016**, *24*, 15590.

[9] J. Macario, P. Yao, S. Shi, A. Zablocki, C. Harrity, R. D. Martin, C. A. Schuetz, D. W. Prather, *Opt. Express* **2012**, *20*, 23623.

[10] A. Rao, S. Fathpour, *IEEE J. Sel. Top. Quant.* **2018**, *24*, 1.

[11] A. Rao, A. Patil, P. Rabiei, A. Honardoost, R. DeSalvo, A. Paolella, S. Fathpour, *Opt. Lett.* **2016**, *41*, 5700.

[12] A. Bartasyte, S. Margueron, T. Baron, S. Oliveri, P. Boulet, *Adv. Mater. Interfaces* **2017**, *4*, 1600998.

[13] G. Poberaj, H. Hu, W. Sohler, P. Günter, *Laser Photonics Rev.* **2012**, *6*, 488.

[14] J. Chiles, S. Fathpour, *Optica* **2014**, *1*, 350.

[15] J. Thomas, M. Heinrich, P. Zeil, V. Hilbert, K. Rademaker, R. Riedel, S. Ringleb, C. Dubs, J.-P. Ruske, S. Nolte, A. Tünnermann, *Phys. Status Solidi (a)* **2011**, *208*, 276.

[16] C. Vannahme, D. Büchter, H. Herrmann, H. Suche, H. Hu, R. Nouroozi, R. Ricken, S. Reza, S. Orlov, V. Quiring, *Opt. Photonics News* **2008**, *19*, 24.

[17] E. Saglamyurek, N. Sinclair, J. Jin, J. A. Slater, D. Oblak, F. Bussieres, M. George, R. Ricken, W. Sohler, W. Tittel, *Nature* **2011**, *469*, 512.

[18] A. S. Solntsev, T. Liu, A. Boes, T. G. Nguyen, C. W. Wu, F. Setzpfandt, A. Mitchell, D. N. Neshev, A. A. Sukhorukov, *Appl. Phys. Lett.* **2017**, *111*, 261108.

[19] F. Chen, *J. Appl. Phys.* **2009**, *106*, 11.

[20] H. Jin, F. M. Liu, P. Xu, J. L. Xia, M. L. Zhong, Y. Yuan, J. W. Zhou, Y. X. Gong, W. Wang, S. N. Zhu, *Phys. Rev. Lett.* **2014**, *113*, 103601.

[21] L. Novotny, N. van Hulst, *Nat. Photonics* **2011**, *5*, 83.

[22] J. M. Lee, J. Lim, N. Lee, H. I. Park, K. E. Lee, T. Jeon, S. A. Nam, J. Kim, J. Shin, S. O. Kim, *Adv. Mater.* **2015**, *27*, 1519.

[23] X. Lan, Q. Wang, *Adv. Mater.* **2016**, *28*, 10499.

[24] N. J. Halas, S. Lal, S. Link, W. S. Chang, D. Natelson, J. H. Hafner, P. Nordlander, *Adv. Mater.* **2012**, *24*, 4842.

[25] H. Chen, L. Shao, Q. Li, J. Wang, *Chem. Soc. Rev.* **2013**, *42*, 2679.

[26] K. S. Lee, M. A. El-Sayed, *J. Phys. Chem. B* **2006**, *110*, 19220.

[27] G. Baffou, R. Quidant, *Laser Photonics Rev.* **2013**, *7*, 171.

[28] W. Zhou, X. Gao, D. Liu, X. Chen, *Chem. Rev.* **2015**, *115*, 10575.

[29] K. Y. Choi, G. Liu, S. Lee, X. Chen, *Nanoscale* **2012**, *4*, 330.

[30] P. Wang, B. Huang, Y. Dai, M. H. Whangbo, *Phys. Chem. Chem. Phys.* **2012**, *14*, 9813.

[31] R. Weissleder, M. Nahrendorf, M. J. Pittet, *Nat. Mater.* **2014**, *13*, 125.

[32] X. Zhang, Y. L. Chen, R. S. Liu, D. P. Tsai, *Rep. Prog. Phys.* **2013**, *76*, 046401.

[33] S. Sarina, E. R. Waclawik, H. Zhu, *Green Chem.* **2013**, *15*, 1814.

[34] X. F. Liu, Q. B. Guo, J. R. Qiu, *Adv. Mater.* **2017**, *29*, 1605886.

[35] S. Wang, Y. Zhang, J. Xing, X. Liu, H. Yu, A. Di Lieto, M. Tonelli, T. C. Sum, H. Zhang, Q. Xiong, *Appl. Phys. Lett.* **2015**, *107*, 161103.

[36] D. Wu, J. Peng, Z. Cai, J. Weng, Z. Luo, N. Chen, H. Xu, *Opt. Express* **2015**, *23*, 24071.

[37] Z. Kang, M. Y. Liu, X. J. Gao, N. Li, S. Y. Yin, G. S. Qin, W. P. Qin, *Laser Phys. Lett.* **2015**, *12*, 045105.

[38] X.-D. Wang, Z.-C. Luo, H. Liu, M. Liu, A.-P. Luo, W.-C. Xu, *Appl. Phys. Lett.* **2014**, *105*, 161107.

[39] M. C. Ridgway, R. Giulian, D. J. Sprouster, P. Kluth, L. L. Araujo, D. J. Llewellyn, A. P. Byrne, F. Kremer, P. F. Fichtner, G. Rizza, H. Amekura, M. Toulemonde, *Phys. Rev. Lett.* **2011**, *106*, 095505.

[40] S. Wolf, J. Rensberg, A. Johannes, R. Thomae, F. Smit, R. Neveling, M. Moodley, T. Bierschenk, M. Rodriguez, B. Afra, S. Bin Hasan, C. Rockstuhl, M. Ridgway, K. Bharuth-Ram, C. Ronning, *Nanotechnology* **2016**, *27*, 145202.

[41] O. Pena-Rodriguez, A. Prada, J. Olivares, A. Oliver, L. Rodriguez-Fernandez, H. G. Silva-Pereyra, E. Bringa, J. M. Perlado, A. Rivera, *Sci. Rep.* **2017**, *7*, 922.

[42] H. Amekura, S. Mohapatra, U. B. Singh, S. A. Khan, P. K. Kulriya, N. Ishikawa, N. Okubo, D. K. Avasthi, *Nanotechnology* **2014**, *25*, 435301.

[43] A. A. Leino, O. H. Pakarinen, F. Djurabekova, K. Nordlund, P. Kluth, M. C. Ridgway, *Mater. Res. Lett.* **2013**, *2*, 37.

[44] R. Carles, C. Farcau, C. Bonafos, G. Benassayag, M. Bayle, P. Benzo, J. Groenen, A. Zwick, *ACS Nano* **2011**, *5*, 8774.

[45] S. J. Henley, M. J. Beliatis, V. Stolojan, S. R. Silva, *Nanoscale* **2013**, *5*, 1054.

[46] T. Cesca, B. Kalinic, N. Michieli, C. Maurizio, A. Trapananti, C. Scian, G. Battaglin, P. Mazzoldi, G. Mattei, *Phys. Chem. Chem. Phys.* **2015**, *17*, 28262.

[47] S. Wolf, J. Rensberg, A. Johannes, R. Thomae, F. Smit, R. Neveling, M. Moodley, T. Bierschenk, M. Rodriguez, B. Afra, *Nanotechnology* **2016**, *27*, 145202.

[48] A. L. Stepanov, *Rev. Adv. Mater. Sci.* **2011**, *27*, 115.

[49] W. Nie, Y. Zhang, H. Yu, R. Li, R. He, N. Dong, J. Wang, R. Hübner, R. Böttger, S. Zhou, H. Amekura, F. Chen, *Nanoscale* **2018**, DOI: 10.1039/c7nr07304f.

[50] Y. Sun, Y. Bai, D. Li, L. Hou, B. Bai, Y. Gong, L. Yu, J. Bai, *Opt. Express* **2017**, *25*, 21037.

[51] A. S. Mayer, C. R. Phillips, C. Langrock, A. Klenner, A. R. Johnson, K. Luke, Y. Okawachi, M. Lipson, A. L. Gaeta, M. M. Fejer, *Phys. Rev. Appl.* **2016**, *6*, 054009.

[52] J. F. Ziegler, J. P. Biersack, U. Littmark, *The Stopping and Range of Ions in Solids*, Pergamon, New York **1985**.

[53] F. Chen, H. Hu, J. H. Zhang, X. D. Liu, B. R. Shi, F. Lu, K. M. Wang, *Mater. Sci. Eng. B* **2001**, *86*, 15.

[54] M. A. Yurkin, A. G. Hoekstra, *J. Quant. Spectroscra.* **2011**, *112*, 2234.

[55] G. Mie, *Ann. Phys.* **1908**, *25*, 377.

[56] S. Zhang, N. Dong, N. Mcevoy, M. O'Brien, S. Winters, N. C. Berner, C. Yim, Y. Li, X. Zhang, Z. Chen, *ACS Nano* **2015**, *9*, 7142.

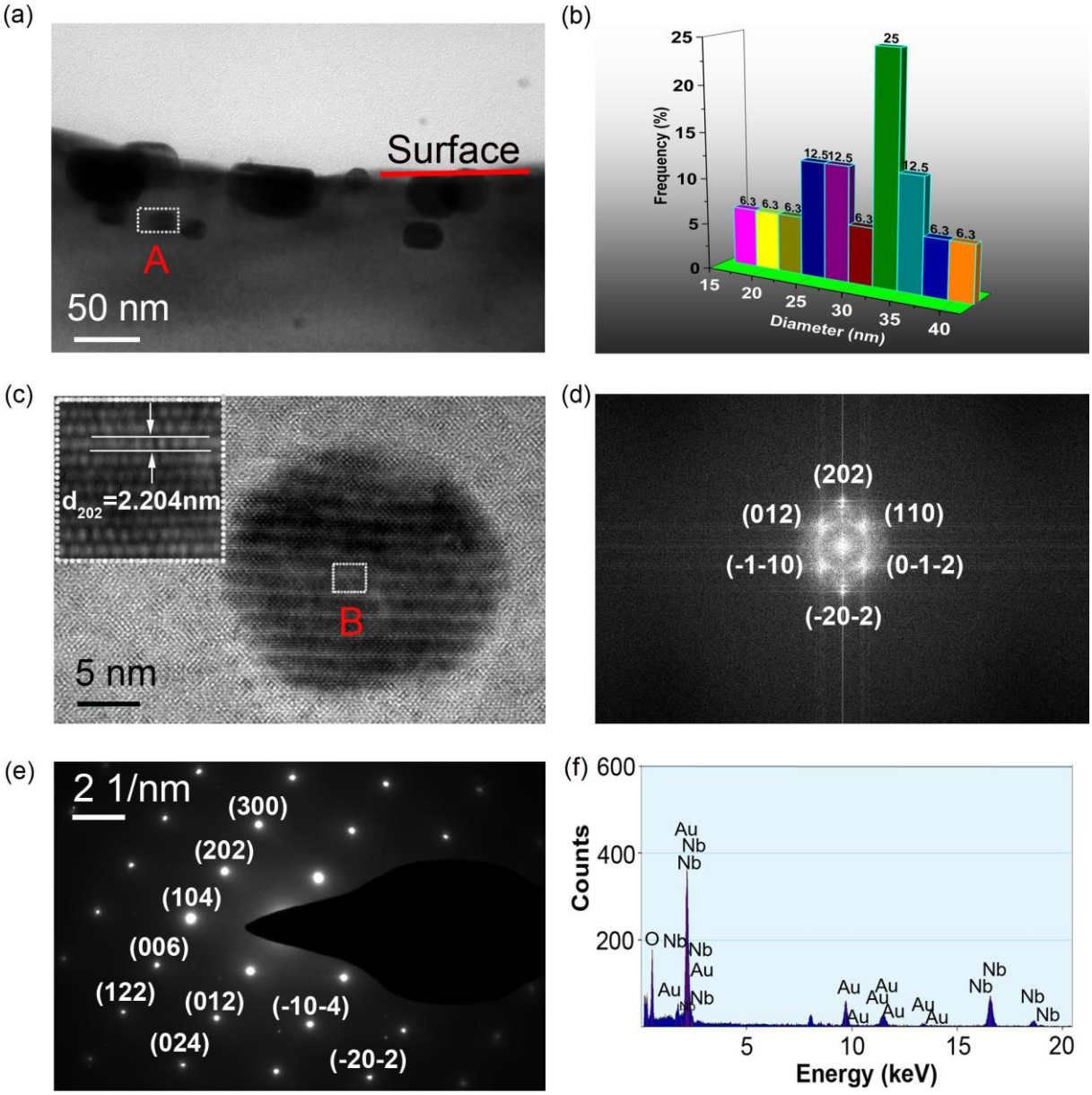

Figure 1. Images of TEM. a) XTEM image of the sample and the SAED pattern corresponding to the circular area labeled as A. b) Size histogram showing the diameter distribution of NPs obtained from the XTEM image. c) HRTEM images of the selected NPs corresponding to the rectangular areas labeled as A; Insert is local enlarged image corresponding to the rectangular areas labeled as B. d) FFT patterns corresponding to HRTEM images of the NPs. e) SAED pattern corresponding to the circular area labeled as A. f) EDX spectrum obtained from the implanted region.

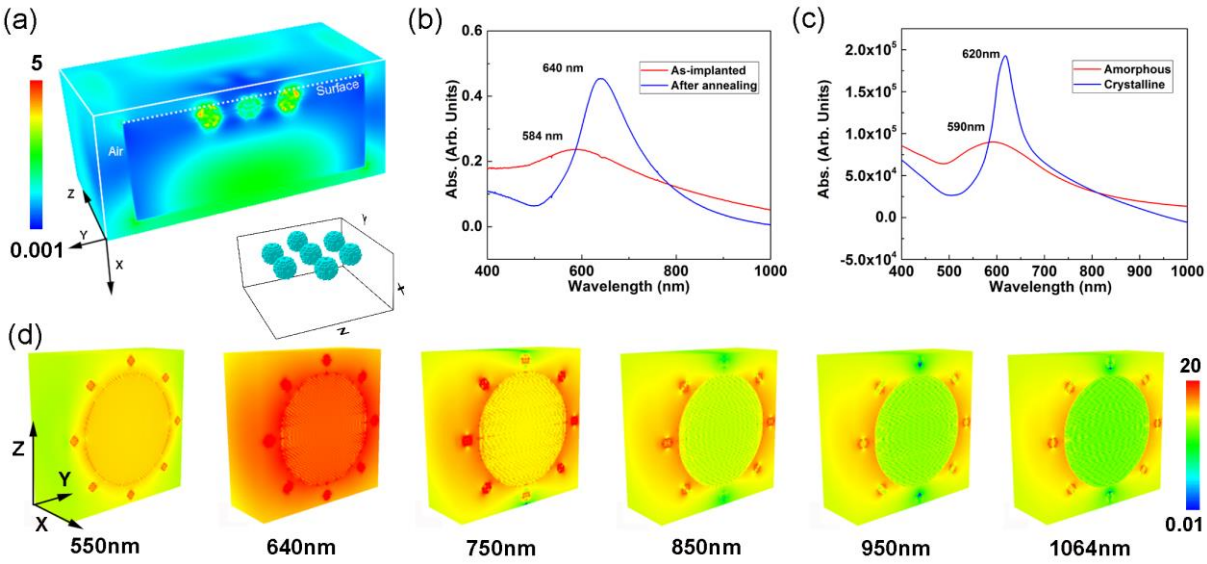

Figure 2. Measurement and simulation of the SPR absorption and the near filed distribution. a) near filed distribution of NPs with 30 nm diameter in the $LiNbO_3$ crystal. SPR absorption of experiment b) and measurement c). d) Near filed distribution under different wavelength.

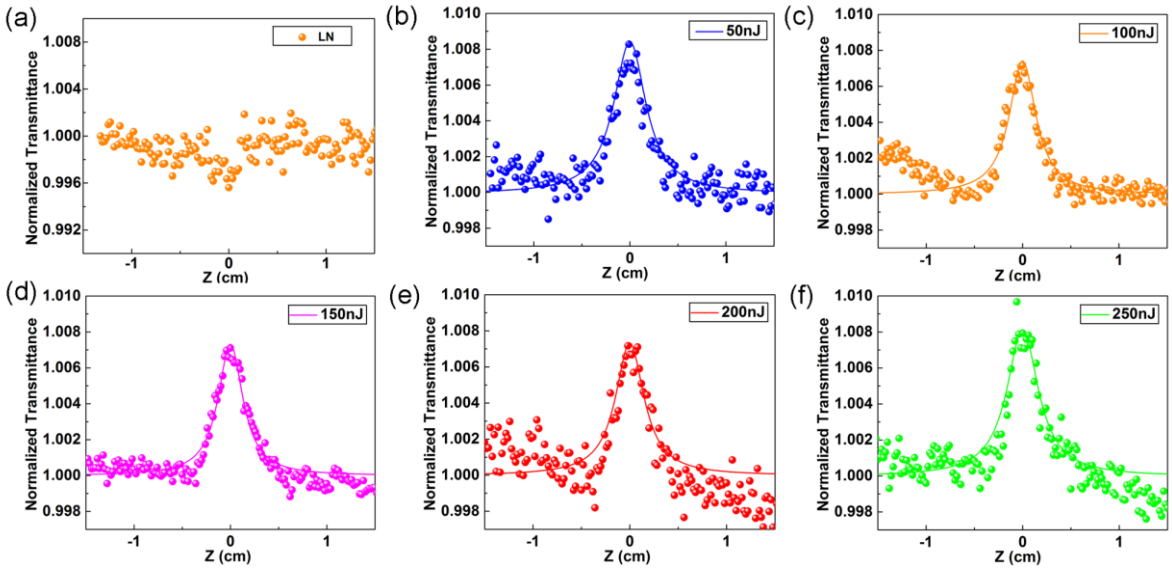

Figure 3. Measurement of the open-aperture Z-scan. a) Open-aperture Z-scan results of $LiNbO_3$ under 340 fs at 1030 nm. b)- f) Open-aperture Z-scan results of the sample under 340 fs at 1030 nm with different pulse energies.

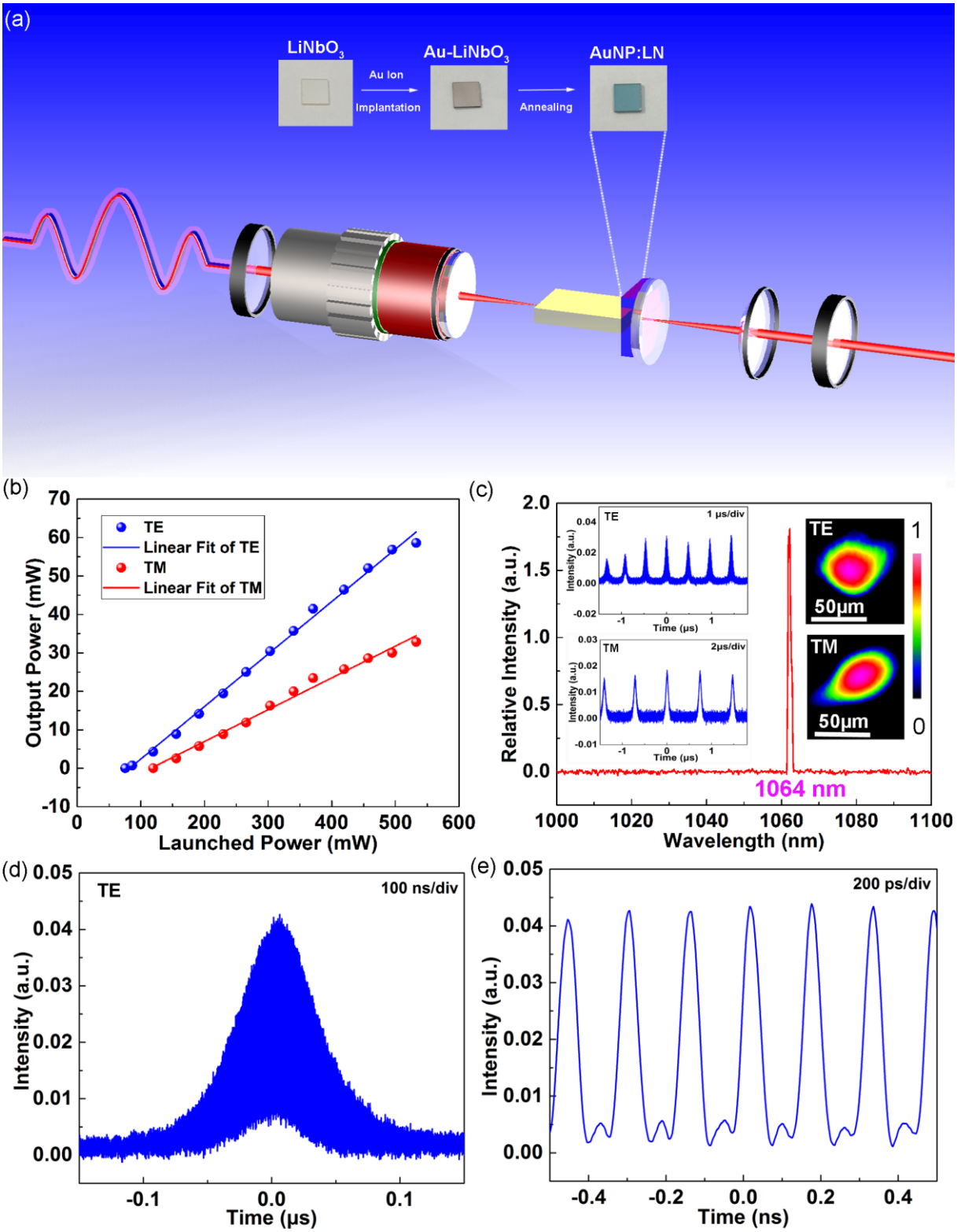

Figure 4. Characterization of Q-switched mode-locking. a) Schematic diagram of the experimental arrangement for the Q-switched mode-locking generation. b) The output power as a function of launched power. c) Emission spectrum at 1064 nm. Insert shows the pulse trains and near-filed modal profiles from waveguide at TE- and TM-polarized light pump. d) Q-switched pulse envelopes. e) Mode-locked pulse train.

Table 1.

Energy [nJ]	50	100	150	200	250
Nonlinear absorption coefficients [cm/GW]	-130.25	-46.94	-28.51	-24.57	-24.24

Nonlinear absorption coefficients of the sample under the excitation at different pulse energies.

Au nanoparticles in $LiNbO_3$ crystals prepared by ion implantation, a well-developed microelectronic-chip technology, enabling considerable saturable absorption at NIR wavelength of 1μm. With this feature the $LiNbO_3$ wafer embedded with Au nanoparticles has been applied as efficient saturable absorber for mode-locking, generating 74.1-ps laser pulses at 1 μm.

Keyword
plasmonic Au nanoparticles, lithium niobate crystals, ion implantation, saturable absorbers, mode-locked lasers

C. Pang, R. Li, Z.Q. Li, N.N. Dong, C. Cheng, W.J. Nie, R. Böttger, S.Q. Zhou, J. Wang, F.

Chen*

Title Lithium niobate crystal embedded with Au nanoparticles: A new saturable absorber for efficient mode-locking of ultrafast laser pulses at 1μm

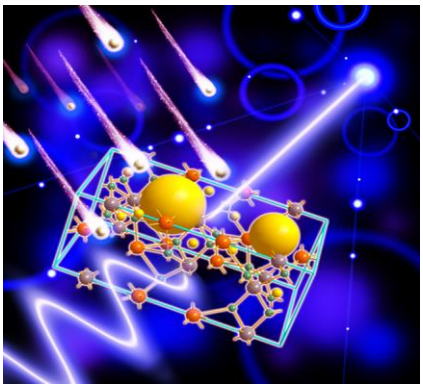

Supporting Information

Title Lithium niobate crystal embedded with Au nanoparticles: A new saturable absorber for efficient mode-locking of ultrafast laser pulses at 1μm

*Chi Pang, Rang Li, Ziqi Li, Ningning Dong, Chen Cheng, Weijie Nie, R. Böttger, Shengqiang Zhou, Jun Wang, and Feng Chen**

1. Au^+ depth distributions simulated by SRIM

Figure S1 diaplays the depth distributions simulated by SRIM with fluences of 3×10^{16} ions/cm^2. The result indicates a Gaussian-like density distribution of Au^+ ions versus depth below the surface of irradiated samples. It is worth noting that the distribution center of Au^+ ions is 44 nm, with a total range of around 100 nm. In general, the higher densities of ions make the larger NPs. However, the simulated result is not agreed with the reality from TEM image, in which most NPs with large scale distribute in the near surface, that may be due to the movement of NPs during the annealing process.[1]

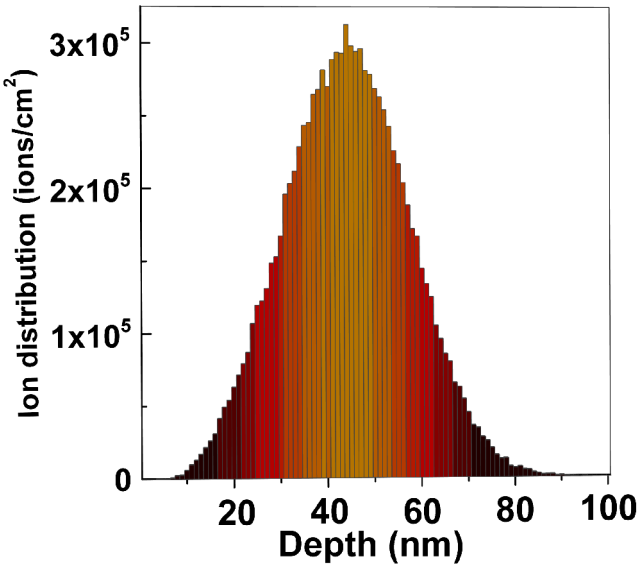

Figure S1. Au^+ ion distribution simulated by the SRIM code.

2. Simulation of absorption spectrum

Considering the amorphous and recrystallized process before and after annealing, the absorption spectra of NPs with different diameters are simulated with the refractive indexes obtained from reference 2.1 (in amorphous $LiNbO_3$) and 2.3 (in crystalline $LiNbO_3$)as shown in **Figure S2a** and **b**, respectively.[2,3] Peaks of absorption spectra of NPs are 590 nm and 620 nm in amorphous and crystalline $LiNbO_3$, which are in good agreement with the experiment results as shown in **Figure S2c**.The reason, we surmise, for the little difference of the position of peaks is that the interaction between NPs is ignored in the process of simulation by Mie theory since the size effect is not crucial as shown in **Figure S2a** and **b**. It also can be proved by the difference of simulated absorption spectra of NPs (**Figure S2d**) compared with counterparts of measurement. The absorption spectrum of NPs after annealling (blue line) is the result of simulation by using NPs with diameter of 30 nm, which is the average diameter of NPs from the image of TEM. While the red line reveals the absorption sprctrum of NPs with diameter 2 nm without annealing based on Mie theory, which is perpormed by constantly optimizing parameters. Obviously, the simulation is not consist with the result of measurement. In consequence, based on the conclusion obtained from **Figure 2d**, we introduce an influence factor a_i of NPs with diameter i to fit the absorption γ_{sum}. Besides, **Figure 2d** also gives the fact that NPs with different scales have different effects at different band. Considering this precondition and the fact that the calculated peak position is accurate, the simulation of the whole absorption spectrum is carried out before and after 640 nm separately to simplify calculation.[4]

$$\gamma_i = \frac{18\pi p \varepsilon_d^{3/2}}{\lambda_0} \frac{\varepsilon_m^{"}}{|\varepsilon_m + 2\varepsilon_d|^2} \tag{1}$$

$$\sum a_i \gamma_i = \gamma_{sum} \tag{2}$$

With the optimization of a_i to reduce the error of experiment and simualtion results, the final simulation results are depicts in **Figure S2e** and the parameters are displayed in **Table S1**. The absorption sprctrum without annealing can be simulated by using NPs with diamaters of 2 nm in amorphous $LiNbO_3$, while the counterpart after annealing can be simulated by NPs with three kinds of diameters, which is in accordance with the distribution of diameters of NPs by TEM. In a certain degree of approximation, the values of a_i are 0.8, 0.5, 0.4 for diamaters of 0.5 nm, 1 nm, 2 nm. While, as for the absorption spectrum of the range after 640 nm, a_i can be simulated to be0.1, 2.1, 0.24 for diameaters of 0.5 nm, 1 nm, 2 nm.

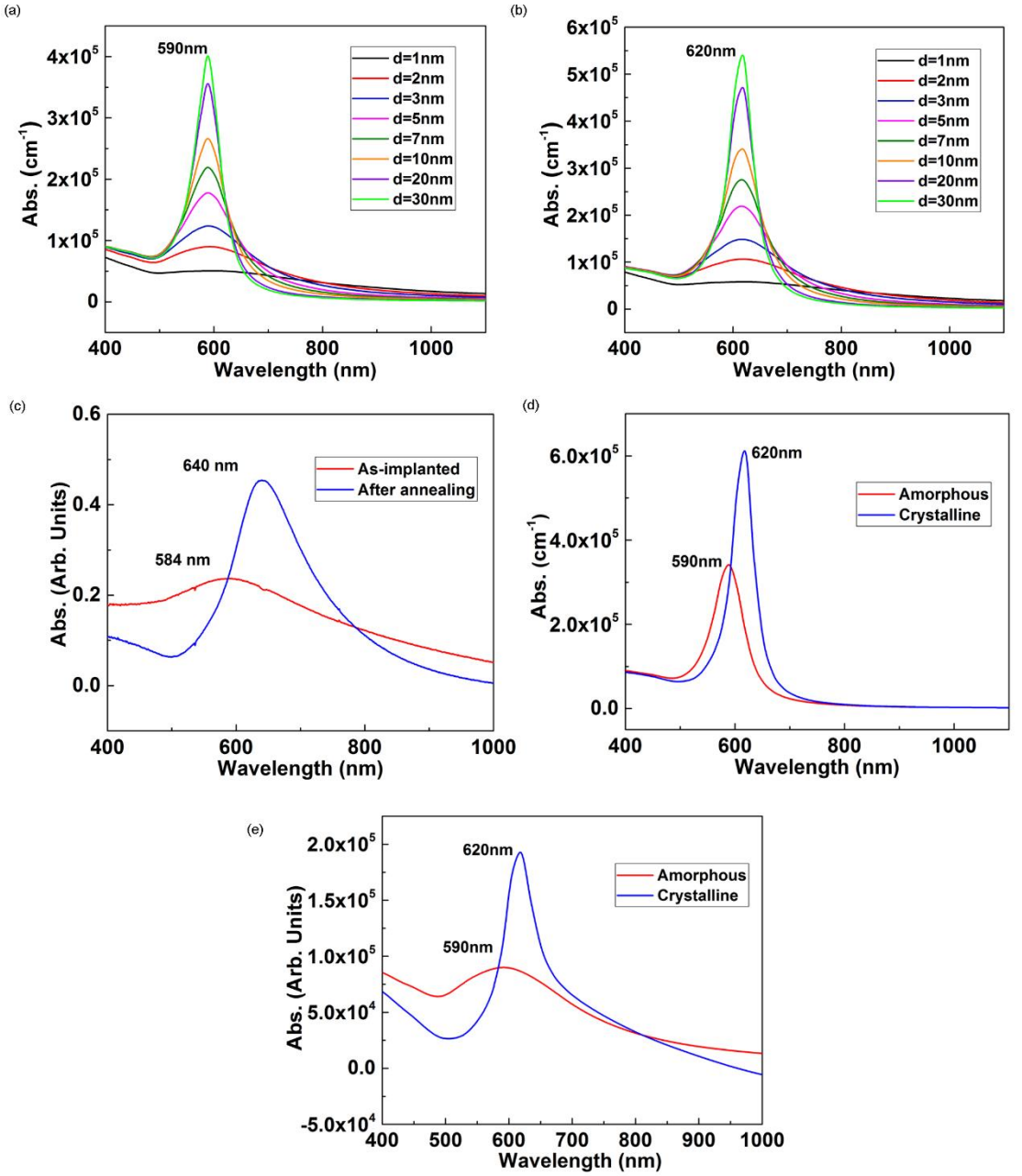

Figure S2. Absorption spectra measured and simulated. Absorption spectra of NPs with different diameters in amorphous a) and crystalline b) $LiNbO_3$. c)Absorption spectra measured before and after annealing. d) Simulated absorption spectra of NPs with separate diameters based on Mie theory. e) Simulated absorption spectrum of NPs with multi-diameters model.

Table S1.

Range of Absorption spectrum [nm]	$a_{0.5}$	a_1	a_2
400-640	0.8	0.5	0.4
640-1000	0.1	2.1	0.24

3. Characterization of nonlinear optical response

Figure S3 displays the result of Z-scan measurement under 515 nm and 1030 nm laser pump with energy of 100 nJ. As shown in **Figure S3a**, the nonlinear response of $LiNbO_3$ embeded Au NPs is larger compared with pure $LiNbO_3$, that is due to the saturation absorption of Au NPs at 515 nm (**Figure S2c**), counteracting reverse saturation absorption of pure $LiNbO_3$ in some extent. **Figure S3b** and **c** shows the result of open-aperture Z-scan at 1030 nm. **Figure S3c** displays pure $LiNbO_3$ shows no obvious nonlinear optical response, while AuNP:LN shows saturation absorption, which indicates that Au NPs have saturation absorption revealed in **Figure S3b**. All of these indicate the synergistic effect between $LiNbO_3$ and Au NPs.

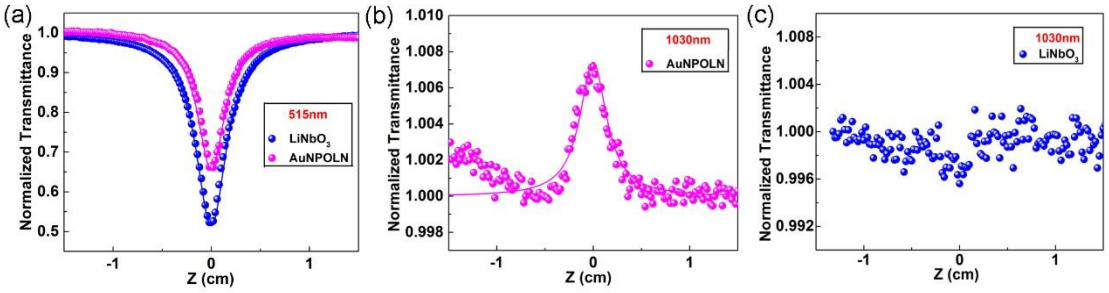

Figure S3. Result of open-aperture Z-scan measurement at the energy of 100 nJ. a) Result of Z-scan for $LiNbO_3$ and AuNP:LN at 515nm. b) Result of Z-scan measurement for AuNP:LN at 1030 nm. c) Result of Z-scan measurement for $LiNbO_3$ at 1030 nm.

4. Characterization of Q-switched pulsed laser

In order to further investigate the pulse features of Q-switched waveguide laser based on the Au NPs as SA. The pulse energy, peak power, pulse duration as well as maximum repetition rates are measured as shown in **Figure S4** at TE and TM polarization, separately. **Figure S4a** displays the dependences of pulse energy and peak power as a function of launched power. With the increase of launched power, the pulse energy increases from 3.9 nJ to 7.4 nJ (from 0 nJ to 7.9 nJ) and the maximum peak power reaches to 139.4 mW (151.0 mW) in TE- (-TM) polarizations. **Figure S4b** shows the variation of the pulse duration and repetition rate under rising launched power. Take parameters in TE-polarization as an example. As the launched power increases, the pulse duration values present the decline on the whole (from 88.3 ns to 53 ns) whilst the repetition rates grow correspondingly (from 3.4 MHz to 7.0 MHz), which is typical and reasonable for passively Q-switched lasers. Counterparts of parameters at TM-polization also reveals a similar result.

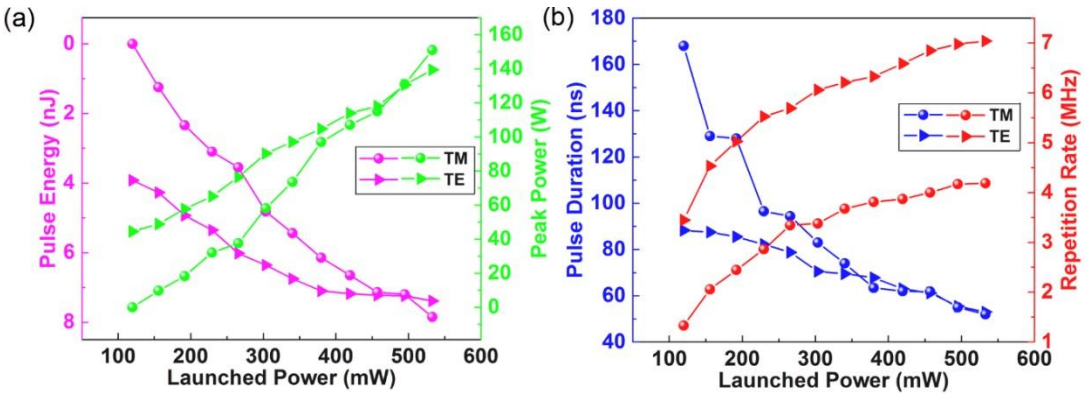

Figure S4. a) The pulsed laser parameters of pulse energy and peak power, and b) values of pulse durations and repetition rates, in TE- and TM-polarization.

5. Schematic of Z-scan system

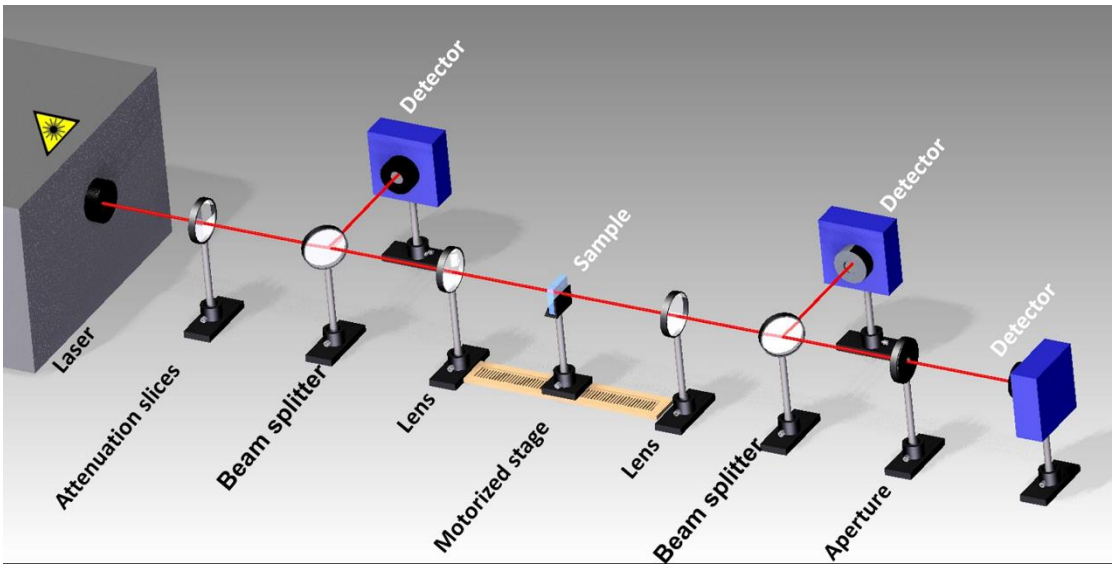

Figure S5. The schematic of the experimental arrangement of the Z-scan system.

This is our schematic of experimental arrangement of the Z-scan system.

References

[1] Y. Shen, L. Zhang, Z. Li, X. Zhang, D. Zhang, X. Li, Z. Wang, B. Yuan, M. Li, C. Liu, *Appl. Surf. Sci.* **2010**, *256*, 3767.

[2] J. Olivares, G. García, F. Agulló-López, F. Agulló-Rueda, A. Kling, J. C. Soares, *Appl. Phys. A-Mater.* **2005**, *81*, 1465.

[3] D. E. Zelmon, D. L. Small, D. Jundt, *J. Opt. Soc. Am. B* **1997**, *14*, 3319.

[4] G. Mie, *Ann. Phys.* **1908**, *25*, 377.